Gallium Plasmonics: Deep Subwavelength Spectroscopic Imaging of Single and Interacting Gallium Nanoparticles

Mark W. Knight,[1] Toon Coenen,[1] Yang Yang,[2] Benjamin J.M. Brenny,[1]

Maria Losurdo,[3] April S. Brown,[4] Henry O. Everitt,[2,4,5] Albert Polman[1,]*

[1] Center for Nanophotonics, FOM Institute AMOLF, Science Park Amsterdam 104, 1098 XG Amsterdam, The Netherlands

[2] Department of Physics, Duke University, Durham, North Carolina 27708, United States

[3] Institute of Inorganic Methodologies and of Plasmas-CNR, and INSTM, via Orabona, 4-70126 Bari, Italy

[4] Department of Electrical and Computer Engineering, Duke University, Durham, North Carolina 27708, United States

[5] Army Aviation & Missile RD&E Center, RDMR-WDS, Redstone Arsenal, Alabama 35898, United States

KEYWORDS: gallium, cathodoluminescence, nanoparticles, ultraviolet, hyperspectral, plasmonics, dielectric function

*** Corresponding Author:** Albert Polman (polman@amolf.nl)

ABSTRACT

Gallium has recently been demonstrated as a new plasmonic material offering UV tunability, facile synthesis, and a remarkable stability due to its thin, self-terminating native oxide. However, dense irregular nanoparticle (NP) ensembles fabricated by molecular-beam epitaxy make characterization of individual particles challenging. Here we employ hyperspectral cathodoluminescence (CL) microscopy to characterize the response of single Ga NPs within an ensemble - characterized by a Gaussian size distribution with mean diameter 72 ± 15 nm - by spatially and spectrally resolving both in-plane and out-of-plane plasmonic modes. These modes, which include hybridized dipolar and higher-order terms due to phase retardation and substrate interactions, are correlated with finite difference time domain (FDTD) electrodynamics calculations that consider the Ga NP contact angle, substrate, and native Ga/Si surface oxidation. This study experimentally demonstrates that single Ga nanoparticles support size-tunable plasmonic resonances and confirms that hybridized plasmonic modes between interacting Ga nanoparticles can produce strong hot spots in the ultraviolet. These properties enable new plasmonic applications, such as simultaneous surface-enhanced Raman spectroscopy, fluorescence, and environmental remediation.

Table of Contents Graphic

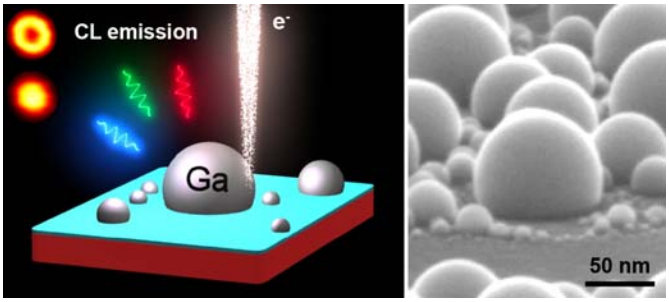

INTRODUCTION

Gallium, a liquid metal near room temperature, has become a key element in both electronic and optoelectronic devices since the start of the microelectronics revolution in the 1960's.[1] In the past several years, Ga has emerged as a promising new material for plasmonics among a growing family of alternative materials.[2,3] Gallium stands out for its complementary material properties compared with the noble metal nanoparticles (NPs). Unlike noble Au and seminoble Ag, gallium is both environmentally stable and has a Drude-like dielectric function extending from the vacuum ultraviolet through the visible and – in the liquid state – infrared spectral regions. With a bulk plasma frequency of 14 eV,[4,5] the excitation of bound, coherent oscillations of conduction electrons on the Ga surface – called a localized surface plasmon resonance (LSPR) – is possible within the broad bandwidth over which gallium is metallic.

These material properties have become relevant for plasmonic applications due to a range of new, bottom-up fabrication techniques capable of producing pure Ga NPs. These methods include self-assembly during molecular beam epitaxy (MBE),[6,7] optically-regulated self-assembly,[8] thermal evaporation,[9] and colloidal synthesis.[10] When exposed to atmosphere following synthesis, Ga NPs form a thin, self-terminating native oxide shell that protects the pure metallic core. This Ga_2O_3 oxide layer,[11] which is 0.5 – 3 nm thick, [10–12] provides both structural and chemical stability, allowing the optical response of Ga NPs to remain stable over many months or years.[7,10] This stability exceeds other UV-compatible plasmonic materials including silver, which lacks a passivating native oxide, and aluminum.[13,14]

Already, novel applications have been demonstrated that rely on the unique optical and material properties of Ga NPs: UV spectroscopy substrates for simultaneous fluorescence and surface-enhanced Raman spectroscopy (SERS),[15] highly compact solid-liquid phase change

memory elements,[16–18] phase transition nonlinear substrates,[19] and graphene/plasmon nanocomposites.[20] While these initial demonstrations are promising, developing the next generation of Ga plasmonic systems requires single particle measurements to gain an understanding of this new material system in the limit of single and interacting NPs both with and without an oxide shell, and in both the solid and liquid phases. For noble metal plasmonics, which rely heavily on oxide-free solid Au, this fundamental understanding has been a critical factor enabling the explosive growth of applications relying on an engineered optical response. To date, obtaining single particle data for Ga has been complicated by fabrication processes that produced densely packed particle arrays with significant size distributions >20%.[7] Within such arrays, standard optical microscopy techniques – such as darkfield spectroscopy – cannot resolve single particles as the interparticle separation lies substantially below the far-field diffraction limit. Recent progress in synthesis has allowed the preparation of colloidal particles with size distributions of 7-8%,[10] although inhomogeneous broadening will still affect the resulting ensemble spectra.

In this work we measure the optical response of individual Ga NPs within a densely packed array using hyperspectral cathodoluminescence (CL) microscopy with deeply subwavelength resolution. Using CL we have nonperturbatively probed the local optical excitability of single particles with diameters between 40 – 140 nm as a function of both spatial position and frequency. To our knowledge this is the first experimental measurement that both spectrally and spatially resolves the optical response of single Ga nanoparticles.

RESULTS AND DISCUSSION

Fabrication and Materials Characterization

Controlled growth of gallium nanoparticle arrays on a silicon substrate was performed using MBE as previously reported (see Methods: Ga NP Fabrication).[6,7] Briefly, Ga was deposited at room temperature under ultra-high vacuum (UHV), where the metal self-assembled into liquid nanoparticles through surface diffusion and Ostwald ripening. The optical properties of the Ga NPs/Si ensemble were monitored in real-time by spectroscopic ellipsometry (SE) and growth was terminated when the LSPR of the effective Ga NPs/Si medium reached the designed wavelength.

For an isolated Ga NP within this ensemble four geometric parameters are sufficient to describe both the structure and local dielectric environment: diameter (D), contact angle (α), and the native oxide thicknesses of gallium (T_{GaOx}) and silicon (T_{SiOx}) (Figure 1A). Both diameter and contact angle can be visualized using high-angle electron micrographs as shown in Figure 1B (see Methods: Structural Characterization). This image also shows the large central Ga NP surrounded by a halo of smaller NPs, a typical feature of Ga NP arrays grown by MBE that is clearly visualized in a normal-incidence image of the sample (Figure 1C).[15] From this image, we extract a size distribution by fitting each particle with a circle using a generalized Hough transform (Figure 1C, inset). The resulting size distribution (N = 387) shows a well-defined peak, and fitting the primary distribution with a Gaussian curve yields a mean diameter of 72 nm ±15 nm . In addition, a large number of small particles, comprising the increasing tail for dimensions below 40 nm, constitute the halo surrounding the larger, isolated particles.

The dielectric function of pure gallium, corresponding to the core of the Ga/Ga_2O_3 core-shell geometry, was determined using spectroscopic ellipsometry (SE) on smooth Ga films. Briefly,

liquid gallium was poured on a glass slide creating a reflective continuous film after which ellipsometric measurements were performed in an inert N_2 atmosphere both at liquid and solid Ga temperatures (see Methods: Measuring Permittivity). Our experimentally inferred permittivity for solid Ga, shown in Figure 1D (circles), agrees well with literature values for the dielectric function of Ga at 300 K.[4,5,21,22] a full comparison spanning the experimental spectral range is provided in Supplemental Materials, along with downloadable dielectric functions (Figure S1). This detailed comparison was performed in the spirit of previous work on plasmonic materials that has noted considerable discrepancies between published dielectric functions.[23] While the full band structure of Ga is complex, the primary features of the solid phase Ga dielectric function can be attributed to Drude-like free electron oscillations in the blue-UV spectral regime, and to interband transitions in the green-red region of the spectrum.[2,4,5] These interband transitions damp plasmonic behavior beyond the visible ($\lambda_0 > 700$ nm) based on the well-known SPP resonance condition ($\varepsilon_r < -2$) for spherical particles.[21,24–26] In the liquid phase, however, gallium behaves as a pure Drude metal from the UV through the near infrared and supports plasmonic resonances over a much broader wavelength range (Figure 1D, crosses).

Spectroscopic ellipsometry on nanoparticle films, performed *in situ* during growth, permits real-time monitoring of the ensemble pseudodielectric function relative to the initial substrate and the bulk dielectric of Ga (Figure 1E). Following the method described in earlier work,[6,21] the ellipsometric parameters Δ and ψ were converted to a pseudodielectric function representing the effective dielectric function of a two phase ambient/sample system.[6,27] Fitting the ellipsometric measurements of the pre-deposition silicon substrate using a two-layer model (SiO_2 on crystalline Si) yields a native oxide thickness of 1.1 ± 0.1 nm.

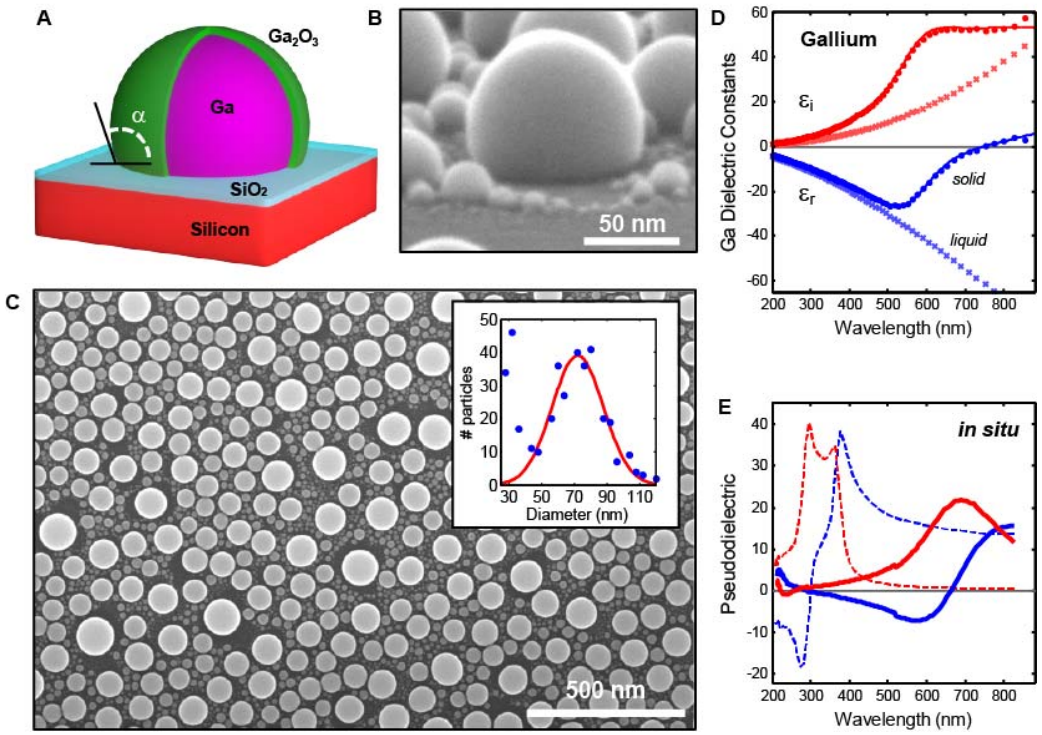

Figure 1. Gallium nanoparticles. **(A)** The geometry of a Gallium nanoparticle can be approximated as a truncated sphere specified by a diameter, contact angle, and oxide thickness. The Si substrate will also have a thin native oxide on the surface. **(B)** Image of a Ga particle taken at 75° tilt with D = 93 nm. **(C)** Typical SEM of a Ga particle array. Inset: the measured size distribution of particles in this image (N = 387) fit with a Gaussian distribution indicating a mean diameter of 72 ± 15 nm. The significant tail for small particles reflects the large number of small Ga particles formed during the fabrication process. **(D)** Experimental dielectric functions of solid Ga (circles) and liquid Ga (crosses), and the multicoefficient FDTD fit used in simulations (lines). **(E)** Pseudodielectric function extracted from ellipsometry measurements on a bare n-Si <111> substrate prior to deposition (dashed lines), and after Ga particle formation (solid lines).

Mapping and Modeling Single Particle Fields

The optical response of the Ga NP film was probed using hyperspectral cathodoluminescence (CL) microscopy, where a complete spectrum of the e-beam induced photoemission is acquired for every pixel in a scan of the sample surface (Figure 2A). To measure CL emission, an energetic beam of 30 keV electrons was focused onto the sample through a small aperture in an Al-coated parabolic mirror. An initial survey scan (Figure 2B) was collected to obtain a high-resolution structural image of the sample and a reference for drift correction during subsequent CL measurements. During a CL scan, both secondary electron emission and optical emission were simultaneously captured for each beam position, with the total photoemission from the sample excited at each position collected by a parabolic mirror, then spectrally dispersed and focused onto a CCD sensor array to measure the local excitability spectrum. This process allows us to construct a hyperspectral 'data cube' containing a complete spectrum for every beam position on the sample. The spatial resolution within a data cube is determined by the electron beam diameter (few-nm), the evanescent electric field of the beam (<20 nm), and the spectral resolution determined by the spectrometer optics (sub-nm). Details on the implementation of our CL system are available in Methods: Cathodoluminescence.

From the hyperspectral data a spatial excitability map may be constructed over any spectral region, and that excitability map can be correlated with a corresponding map of the physical sample geometry (Figure 2C-G). Unlike imaging performed with filters, this method allows the selection of an integration bandwidth during post-processing to balance signal-to-noise and mode discrimination optimally. Four representative excitability maps for Ga NP are shown in Figures 2D-G, with center wavelengths of λ_0 = 380, 430, 500, and 800 nm (bandwidth: 50 nm). These wavelengths were selected to illustrate the dependence of emission wavelength on excitation

location over the range of the spectrometer. It has previously been shown that these excitability maps closely correspond to the z-component of the radiative local density of optical states (LDOS) because the electron beam interacts with the sample through the vertical component of the electric field.[24,28–30] A larger induced local field corresponds to an increased transition probability.[24] Within the spatial map (Figure 2C), six particles are highlighted and assigned the letters *a*-*f*, with corresponding diameters estimated from the survey scan as D = 40, 60, 80, 100, 120, and 140 nm, respectively. This distribution of sizes spans the particle distribution measured in Figure 1C, so analysis of these six NPs can provide a representative understanding of the optical response of this Ga NP ensemble.

These maps show two key features: size-dependent excitability profiles, and a lack of interparticle interactions. At short wavelengths (λ_0 = 380, 430 nm) there are two distinct excitability distributions: annuli (for D > 100 nm), and centered peaks (for D < 100 nm). At longer wavelengths (λ_0 = 500, 800 nm), only weak emission excited near the particle center is observed. For all the particles within these scans, the CL emission is observed to be symmetric around the particle axis of symmetry. This implies that neighboring particles do not perturb the LDOS of individual particles, allowing us to consider them as if they were isolated Ga NPs on an infinite substrate.[31,32] This lack of interaction might be unexpected due to the dense array geometry shown in Figure 1C. However, the growth process itself likely ensures that interparticle interactions remain weak. Prior to the formation of the oxide shell, two liquid Ga particles that touch will coalesce and form a single large particle, making the formation of very closely spaced particles with few-nm gaps unlikely. This observation supports the assertion in previous ellipsometric studies that the ensemble optical response could be well approximated as an amalgam of single-particle responses.[6,7,33]

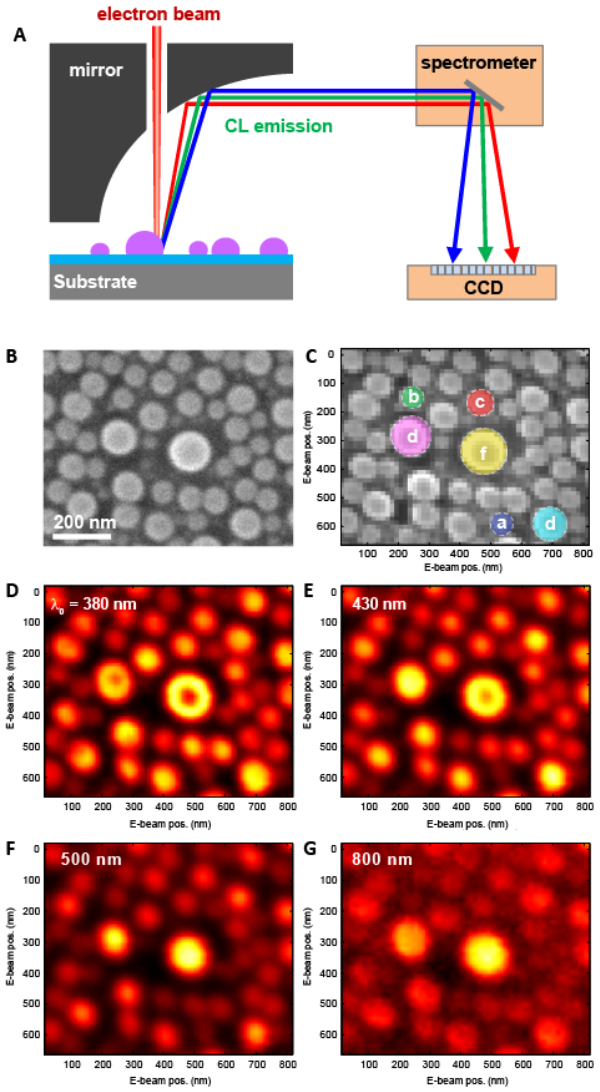

Figure 2. Cathodoluminescence imaging of Ga nanoparticles. **(A)** Schematic of the hyperspectral cathodoluminescence microscopy system. **(B)** Survey scan of the sample area acquired prior to CL imaging. **(C)** Secondary electron image acquired simultaneously with the CL scans. Particles used for subsequent analysis are indicated by letters a-f. From the survey image, the diameters of these particles were determined to be ~40, 60, 80, 100, 120, and 140 ± 5 nm. **(D – G)** CL images at λ_0 = 380, 430, 500, and 800 nm. All images were integrated over a spectral bandwidth of 50 nm, normalized to the full color scale, spatially interpolated for clarity in visualizing the CL distributions.

These two observed excitability distributions – annuli and bright centers – can be understood as either in-plane or out-of-plane dipolar resonances (Fig 3 A,B).[32,34] For a dipole oriented along the sample plane the largest vertical field components will occur at the edges of the dipole. These vertical field components couple to the incident electron beam, exciting the in-plane resonance which subsequently decays and emits the photons comprising the CL signal. Since vertically and horizontally polarized emission was collected with equal probability during measurement, this dipolar field distribution exhibits rotational symmetry in the LDOS and forms the 'annulus' shape seen in Figure 3A for a D = 140 nm Ga NP (Figure 2C, particle *f*). For an out-of-plane dipole the vertical field component is directly excited and will be maximized at the center, which appears in CL as an emission maximum at the particle center (Figure 3B). For clarity, the particle outline is shown by the dashed green circle, with amplitude crosscuts plotted at the position of the two blue lines.

Modeling of these two resonances was performed using the finite-difference time-domain method using experimental dimensions for the particle geometry (see Methods: Computational Modeling). Plane wave simulations do not directly correspond to CL maps, but they allow us to visualize the field distributions and energies of the same resonant modes that are experimentally probed using electron beam excitation. For the simulations in Figure 3, the particle was defined as an oxide-free truncated sphere with D = 140 nm, a contact angle of 110°, and a substrate SiO_2 layer of 1 nm. The dielectric function of the Ga core was modeled using a multicoefficient fit to the experimental dielectric function of solid Ga. While the phase of the Ga core was not directly measured during CL imaging, the Ga phase actually exerts a relatively small effect on either the resonance position or shape in the Drude-like regime, below the onset of interband transitions (Figure S2).[35]

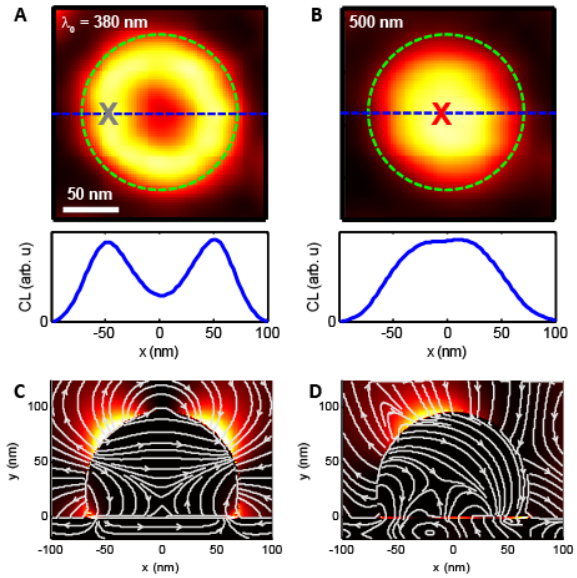

Figure 3. In-plane vs. out-of-plane modes for a *D*=140 nm Ga NP (particle *f*). **(A – B)** CL maps showing a characteristic 'annulus' shape for the in-plane modes (λ=380 nm), and a single maximum for the out-of-plane dipolar modes (λ=500 nm). Crosscuts show normalized field intensities across the particle center (cut position: dashed blue lines). Positions marked by X indicate locations at which nearly pure in-plane or out-of-plane modes may be excited and representative emission spectra can be extracted. **(C – D)** Calculated field maps of E_z^2, which correspond to the experimental maps, are shown at the calculated peak intensities of these modes for (C) normal incidence excitation with λ_0 = 270 nm and (D) a p-polarized wave with λ_0 = 470 nm and at 70° off-normal incidence. Electric field lines are shown in white.

To model the in-plane mode the particle was excited by a linearly polarized, normal incidence plane wave. The in-plane mode can be visualized in these simulations as two lobes in the UV electric field enhancement (Figure 3C). This is shown in a vertical field slice along the polarization axis which shows an E_z^2 distribution matching the annular shape observed in the shortest experimentally accessible CL wavelengths (Figure 3A), which correspond to a tail of the UV particle resonance. The field slice shown in Figure 3C corresponds to the calculated peak

scattering intensity in the UV to show the mode distribution most cleanly (λ_0 = 270 nm). Calculated mode profiles at other wavelengths show that this plasmonic mode distribution spans the UV and blue region of the spectrum (λ_0 < 400 nm) , while the flat bottom of the particle shows many distinct field distributions throughout this range that correspond to a quasi-continuum of narrow band, particle-interface modes that can be viewed as waveguide cavity resonances.[36] Electric field lines (in white) clearly illustrate the dipolar nature of the in-plane plasmonic resonance. Importantly, the out-of-plane dipolar mode cannot be excited in the quasistatic limit in which the particle is much smaller than the impinging light wavelength. Even for finite-sized particles, including the 140 nm particle simulated for these field maps, the out-of-plane mode may only be weakly driven via phase retardation across the particle.

To visualize the field distribution of the vertical mode the particle was also simulated using a grazing incidence p-polarized plane wave. A calculated E_z^2 field slice for λ_0 = 500 nm illustrates the resulting vertical dipolar resonance (Figure 3D). The asymmetry in the field profile relative to the CL measurement is due to both the angle of the driving field (70°) and significant phase retardation across the particle whose diameter of λ_0 / 3.5 is well outside of the quasistatic regime. This asymmetry points to the difference between electron beam and plane wave excitation. While the radiative decay (e.g. photon emission) of plasmonic particles does not depend on the excitation source, excitation efficiency does vary for optical and e-beam illumination. Different excitation methods will, therefore, produce different emission spectra.[24,37]

Single Particle Spectra

Based on the LDOS distributions of these two modes, we can spectrally isolate the vertical (out-of-plane) and horizontal (in-plane) resonances by examining spectra from the particle center and edge, respectively. We will now consider spectra from these positions (indicated by X marks on Figures 3A,B).

For the smallest particle ($D \approx 40$ nm) no difference is observed between spectra taken at the particle edge and center (Figure 4A). This is not a physical effect but simply a consequence of the finite resolution of the CL instrument. For a 30 keV beam the excitability maps have a resolution on the order of 20-40 nm.[24,30] Since the modes are separated by less than half the diameter, the two different resonances cannot be spatially resolved for these smallest particles. Spectra calculated using the experimental geometry of particle *a*, however, clearly show a peak corresponding to normal incidence excitation and an in-plane resonance (Figure 4B). The significant tail on the high-energy side of this peak corresponds to a vertical dipole in the UV (shaded region). While transition radiation (TR) - which occurs when a charged particle crosses a dielectric interface - could also provide such a spectral feature,[16,24] we have accounted for this background signal by subtracting the CL measured within an interstitial region directly adjacent to the measured NP. This removes both TR and incoherent emission from the Si substrate. A local background subtraction was used rather than a separate, Ga-free area of the substrate since the dense Ga NP film blocks a fraction of TR radiation from the Si substrate, making the magnitude of the background dependent on the local sample geometry.

For intermediate particles, with D = 60 – 80 nm, we can resolve distinct spectra for the particle edge and center. The edge spectrum, produced by exciting the in-plane dipolar resonance, redshifts and weakens relative to the tail of the vertical, UV mode. The size tuning observed

from D = 40 – 80 nm is the result of phase retardation across the particle and is reproduced well in the simulations (Figure 4B).[24] Slight differences between the experimental and calculated peak positions are due to uncertainty in the particle dimensions extracted from the SEM survey image. Differences in the relative amplitudes most likely result from the different plasmon mode excitabilities for plane-wave excitation compared to electron beam excitation.

For the largest particles, with D > 100 nm, the spectra from the edge and center are distinct, and we observe the vertical modes (colored lines) shift from the UV into the detection range of our CL system (λ_0 > 350 nm). Rather than a single resonance, this peak is nearly a continuum of resonances resulting from strong interactions between the Ga NPs and the underlying high index Si substrate, which enables the vertical dipolar mode to hybridize with higher-order modes.[33,38–41] At the same time, the dipolar in-plane mode (grey lines) has redshifted out of the plasmonic regime for Ga, and only the tail of a higher-order, multipolar UV resonance is measured (Figure 4B).

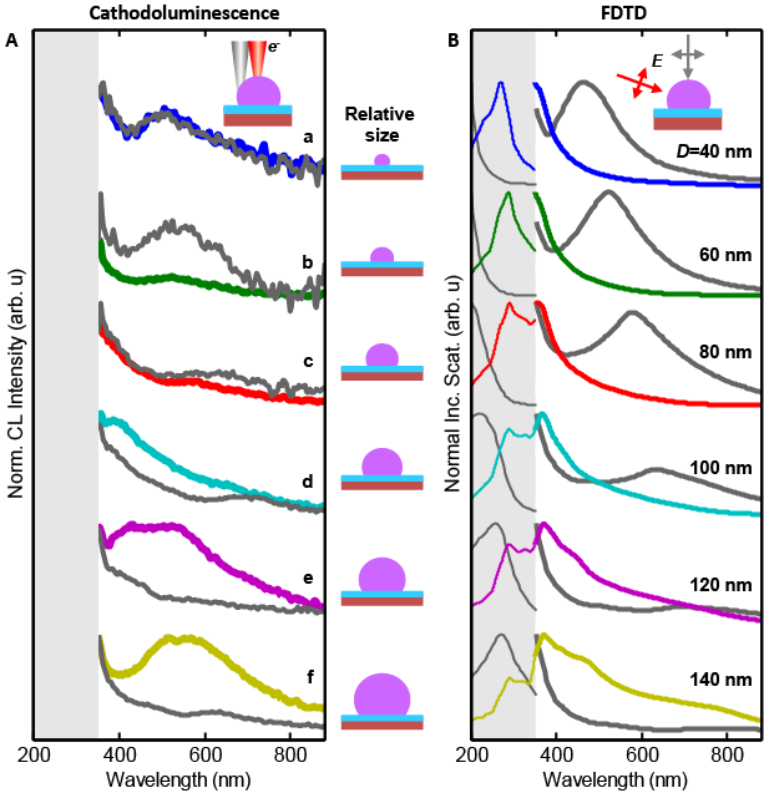

Figure 4. CL spectra of Ga particles**. (A)** Experimental CL spectra for excitation either at the side of the particle (grey lines) or the center of the particle (colored lines). The shadowed area indicates the spectral region inaccessible to the CL detector. **(B)** Spectra calculated for the experimental particle dimensions using FDTD with plane-wave excitation at either normal incidence (grey lines) or grazing incidence (70°, colored lines). All spectra are offset for clarity: thick lines are normalized within the experimental data range, and thin lines are normalized within the λ_0 = 200 – 350 nm UV spectral range (shaded region).

Although reasonable agreement is observed between the measured and calculated spectra, especially considering they were obtained by two different excitation methods, some discrepancies remain between the observed and calculated resonance energies. To understand the origin of these differences we have calculated the spectral influence of the geometrical parameters on the in-plane mode: the Ga_2O_3 shell, the native SiO_2 oxide, and the Ga contact

angle. We find that the Ga oxide shell, which has a refractive index $n_{GaOx} \approx 2$ and a thickness between 0.5 – 3.0 nm,[10–12,42] does not exert a significant influence on the particle spectrum, causing only a negligible redshift (Figure 5A,B). By contrast, the in-plane resonance is strongly influenced by both the presence of the native substrate oxide (Figure 5C,D) and alterations to the contact angle (Figure E,F). Varying each parameter over a small, experimentally relevant range significantly affects relative mode amplitudes and positions: both can shift the visible, in-plane mode by over 100 nm in wavelength.

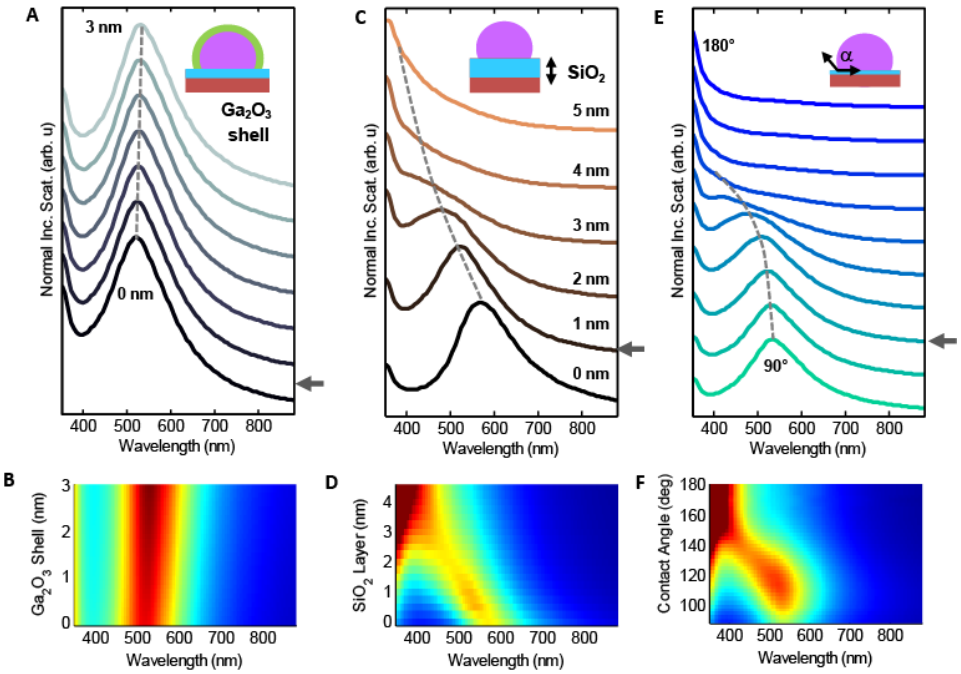

Figure 5. Spectral influence of Ga particle parameters: oxide shell thickness, substrate oxide thickness, and contact angle. Spectra were calculated for a D = 60 nm Ga particle using normal incidence excitation. **(A – B)** Effect of the oxide shell thickness, calculated for 0 nm (unoxidized) to 3 nm with a 1 nm layer of SiO_2 on the Si substrate and a 110° contact angle. **(C – D)** Effect of the native oxide layer on the Si substrate, calculated for 0 – 5 nm, no Ga_2O_3 shell, and a 110° contact angle. **(E – F)** Influence of contact angle on the Ga spectrum, calculated for

angles between 90° (a hemisphere) and 180° (a perfect sphere). The substrate oxide was set at 1 nm, with no Ga_2O_3 shell. Dashed grey lines are provided as a guide to the eye. Grey arrows indicate the parameters used to calculate the NP resonances shown in Figures 3 and 4.

The reason for this sensitivity is the strong interaction between the plasmonic charge oscillations and the high-index silicon substrate. When a plasmonic particle is positioned in vacuum above a dielectric halfspace, an 'image particle' results with a surface charge equivalent to $(\varepsilon - 1)/(\varepsilon + 1)$.[25,39] For silicon, which has a large and strongly dispersive permittivity (Figure 1E, dashed lines), the substrate interaction can be conceptually understood as the hybridization of two Ga dimers separated by an SiO_2-filled nanogap.[38,43–45] Interactions between real and image particles allow higher order (i.e. non-dipolar) modes to couple with the dipolar modes, causing resonances to shift and enabling the excitation of non-dipolar charge distributions by the dipolar field of light.[41] For the normal incidence case shown in Figure 5, increasing either the contact angle or the oxide (nanogap) thickness separates and weakens the NP-image interaction. These parameters were computationally tuned to match the experimental spectral peaks of the smallest NPs ($40 < D < 80$ nm), with the best agreement in peak positions found for a simulated SiO_2 layer of 1.0 nm and a contact angle of 110 degrees. Experimentally, these the SiO_2 thickness was measured to be 1.1 nm by ellipsometry, and the contact angle was estimated to be between 100-130 degrees based on the measured dimensions of angled SEM micrographs and an approximation of the NPs as perfect truncated spheres. Given the sensitivity of the Ga-on-Si system to these geometric parameters, especially the native Si oxide, the agreement between the measured and calculated parameters and mode energies shown in Figure 4 is respectable.

Interacting Ga Nanoparticles

While MBE fabrication generally produces Ga NP ensembles without significant near-field interactions between particles, as shown in Figure 2, a small number of Ga NPs do form strongly interacting clusters. The interaction between these clusters can be significantly influenced by both the relative particle diameters and the contact angle, which will add a vertical offset between the particle equators and in-plane dipolar modes of different sized particles. While the gap spacings were below the ~10 nm resolution of our survey image (Figure 6A), a CL scan within this region (dashed white box) allows us to visualize the modification of the LDOS within interacting clusters compared to the isolated particle case for four nanoparticles with different diameters (Figure 6B). It is important to note that since CL measures only the vertical field component, field enhancements in interparticle 'hot spots' appear in CL as a dark gap bounded by bright particle edges.[46]

At short wavelengths, a strong spatial asymmetry in the CL map is observed: the smaller satellite particles appear as asymmetric dipoles (Figure 6C,D), while the bright 'hot spot' adjacent to the central particle is observed to be wavelength-dependent. For the leftmost satellite particle, this hot spot is strongest near the UV edge of our CL detection range, while the right-most particle exhibits a maximum at 430 nm because it has both a larger diameter and a larger gap. For longer wavelengths, where the vertical mode dominates and dipolar charge oscillations are spatially well separated, we observe a substantial reduction in interparticle coupling (Figure 6E,F). These trends are reproduced well by FDTD calculations that approximate the cluster geometry using diameters from the survey image and interparticle gaps of 5 nm (Figure 6G). For this geometry, the normalized, polarization-averaged $|E_z|^2$ reproduces the experimental observations of coupling-induced LDOS asymmetries at short wavelengths (λ_0 = 380 nm, Figure

6H) and dielectric screening of the electric field at long wavelengths where $\varepsilon_r > -2$ (e.g. λ_0 = 800 nm in Figure 6I).

While occurring infrequently on our sample, engineered arrays of hybridized plasmonic Ga clusters may be important for applications that rely on large electric fields, such as surface enhanced Raman scattering (SERS) which scales as approximately the fourth power of the local field.[47–49] Previous work demonstrating SERS spectroscopy on Ga NP substrates hypothesized that significant enhancements in MBE fabricated substrates occurred between coupled asymmetric dimers,[7,15] a hypothesis supported by Mueller matrix ellipsometry measurements showing nonspecular scattering.[50] The CL measurements shown here are the first direct evidence that this type of asymmetric interparticle coupling occurs in Ga NP ensembles.

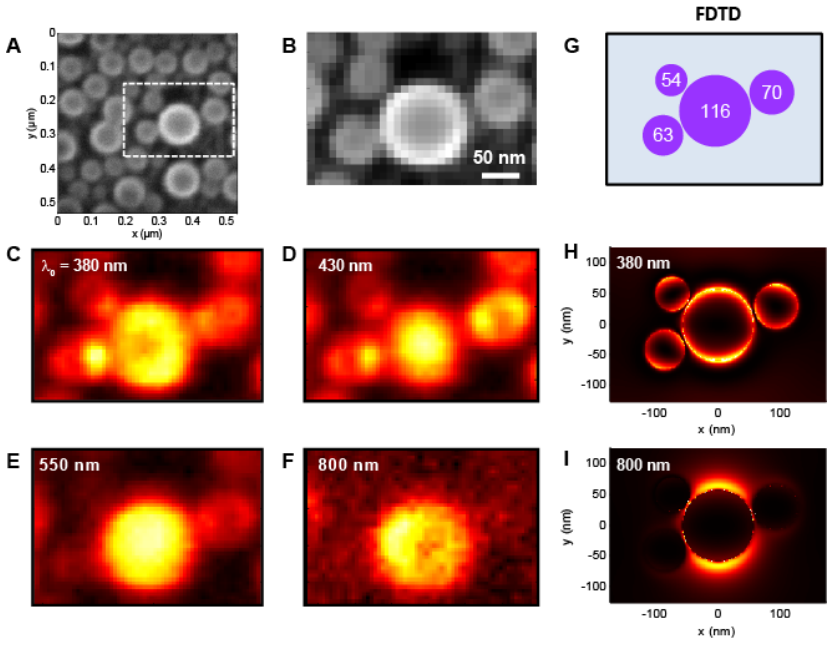

Figure 6. Hybridization in Ga plasmons. **(A)** Survey image with the scan area indicated by the white dashed box. **(B)** Simultaneously acquired SE image of the Ga NP cluster. **(C – F)** CL maps of the cluster at λ_0 = 380, 430, 550, and 800 nm, with an integration bandwidth of 50 nm. **(G)**

Simulation geometry, with particle dimensions indicated. **(H – I)** Simulated in-plane field maps showing polarization-averaged E_z^2. Asymmetries in the field profiles correspond with the CL maps and indicate interparticle interaction.

CONCLUSION

Using hyperspectral cathodoluminescence imaging we have conducted deeply-subwavelength studies of isolated and coupled Ga NP plasmon modes. Individual nanoparticles were observed to exhibit both size tuning and frequency-dependent spatial LDOS profiles. These observed modes were correlated with electrodynamic calculations of the plasmonic mode profiles and the backscattered emission resulting from plasmon decay using experimentally measured Ga dielectric functions for both solid and liquid-phase gallium. At blue and ultraviolet wavelengths we have found that the response of these Ga particles is dominated by an in-plane dipolar oscillation with a position and amplitude strongly influenced by the Si substrate. The long-wavelength response, by contrast, is almost purely determined by a vertical dipolar resonance. We have also offered the first experimental observation of direct Ga interparticle coupling, with measurements of wavelength-dependent hotspots between a large central particle and proximal satellite particles. The high resolution, single particle CL measurements shown here show reasonable agreement with plane-wave modeling based on our experimentally measured dielectric functions. Combined, this study provides a first understanding of single Ga NP resonances from 200-880 nm, spanning the UV through the NIR spectral regime.

METHODS

Ga NP Fabrication. Gallium nanoparticle ensembles were grown by molecular beam epitaxy (MBE) of pure Ga on a 2" wafer of n-type, <111> Si with only a thin native oxide. After a preliminary degas of the Si sample in the MBE load-lock chamber at 200°C, the Si substrate has a residual SiO_2 native oxide thickness of 1.1±0.1 nm. The MBE chamber was maintained under ultra-high vacuum (10^{-11} Torr) during deposition. NP growth took 263 seconds at 300 K resulting in Ga NP in a liquid state.[10,16] During deposition the Ga film self-assembled into nanoparticles through a process of adsorption, surface diffusion, and coalescence through Ostwald ripening.[51,52] Real-time monitoring of this process was performed by *in situ* spectroscopic ellipsometry (SE) from λ_0 = 200 – 820 nm at a 70° angle of incidence, permitting the termination of growth when the desired optical properties were attained (Figure 1E).[6,27] Samples were stored in ambient atmosphere for 21 months prior to the CL measurements, demonstrating the robustness of the native oxide shell.

Structural Characterization. Imaging of individual Ga nanoparticles to measure geometry was performed using a FEG SEM (FEI Verios) with an accelerating voltage of 10 kV and a specimen current of 4.9 pA. Secondary electron emission was measured using an in-column scintillation detector in combination with an immersion lens. To permit observation of the contact angle the sample was tilted at 75°.

Cathodoluminescence. CL imaging was performed using a modified scanning electron microscope (SEM, FEI XL-30). A 30 keV, 800 pA beam of electrons was focused through an Al half-paraboloidal mirror onto a sample with a few-nm spot size. The mirror focus was precisely

aligned to overlap the e-beam impact point, using a custom piezoelectric micromanipulation stage, and the resulting optical emission from the sample was directed to an optical bench attached to the outside of the SEM chamber. The collimated light was then either imaged onto a 1024x1024 Si CCD to ensure proper alignment, or it was fiber-coupled into a spectrometer for analysis. Hyperspectral CL maps were acquired by raster-scanning the e-beam across the sample and recording a raw spectrum for each beam position (per-pixel integration time: 250 ms). Spectroscopy was done using a grating spectrometer (grating: 500 nm blaze, 150 g/mm) with a Si CCD (Princeton Instruments: back-illuminated SPEC-10). Separately, the overall system response was ascertained by dividing the theoretical TR spectrum from aluminum by a measured CL emission spectrum from a single aluminum crystal, where the absence of surface texturing (translational symmetry) prevents the emission of SPPs and only transition radiation (TR) is emitted.[53] The raw gallium spectra were multiplied by this correction factor to account for the properties of the measurement system.

Computational Modeling. The optical response of Ga NPs was modeled using a commercial implementation of the finite-difference time-domain method (FDTD, Lumerical).[54] The simulated NP geometry was specified as an isolated, truncated sphere of diameter *D* forming a contact angle α with an infinite substrate. The material properties of Ga and Si were modeled using broadband multicoefficient fits to experimental dielectric values from the literature.[21,55] The experimental dielectric function used in this work and literature values for the Ga dielectric function are compared in the Supplemental Material and made available for download.[2,5,21] The Ga_2O_3 shell was approximated using the Cauchy dispersion model fit of Rebien *et al.*: $n = n_\infty + B/\lambda^2 + C/\lambda^4$, with $n_\infty = 1.891$, $B = 0.0110\ \mu m^2$, and $C = 0.00048\ \mu m^4$ (with λ in μm).[42]

Particle properties were calculated using the total-field scattered-field (TFSF) formulation where, by separating the simulation domain into regions with either the complete field (at the particle) or only the scattered field (far from the particle), the total power scattered into the far-field by the particle can be calculated. Only power outflow into the upper half-space was included in integrated spectra to facilitate comparison with the hyperspectral CL measurements. For normal incidence plane-wave excitation, spectra and field distributions were calculated using a broadband source. For off-normal excitation, where the source angle in FDTD exhibits frequency dependence, individual spectral points were calculated every 10 nm to permit a well-defined incidence angle (70°) capable of driving out-of-plane modes.[33] The simulation space was discretized using a mesh step of 1 nm within the particle region with a refined mesh dimension of 0.25 nm within the thin oxide layers of both the Ga NP and substrate. Far from the particle, a graded mesh approach increased the mesh step to 4 nm to reduce the computational cost of the simulations without sacrificing accuracy.

Dielectric Function Measurement.

Pure gallium ingots (99.9999% pure) were purchased from GoodFellow. The Ga processing was performed in a glove box purged with N_2 to avoid oxygen atmosphere. Warming the vial liquefied the Ga, which was then poured onto a glass slide at 308 K. The Ga homogeneously wet the glass, forming a smooth, reflective liquid layer. The liquid sample was then transferred to a variable angle spectroscopic UVISEL (Horiba Jobin Yvon) in a continuously purged measurement cell to avoid any atmospheric adsorption or oxidation of the liquid film. Ellipsometric spectra were acquired in the range 190 – 1650 nm to obtain the dielectric function of liquid gallium. In the cell, the sample is mounted on a temperature-controlled holder that was

set to a temperature of 278 K to solidify the Ga film. Subsequently, the ellipsometric spectrum was acquired again to obtain the dielectric function of solid Ga.

The optical constants of gallium were extracted from the measured data using a point-by-point fit, assuming a two layer (Ga-surface / Ga-bulk) model with bulk Ga (5 μm thick) and the rough surface layer modeled using the Bruggeman effective medium approximation (50% Ga, 50% voids).[56]

After ellipsometric measurements the thickness of the solid film was estimated to be ~5 μm, both by microbalance and surface profilometry (Alpha-Step). These methods were used to determine film thickness following optical characterization since the Ga film was significantly thicker than the penetration depth of light. The solid Ga film was also measured by atomic force microscopy and found to have 1.1 nm root mean square (RMS) surface roughness.

The extracted dielectric functions for liquid and solid Ga are plotted in Figure 1D, with a comparison to literature dielectric functions in Figure S1. This comparison shows good agreement between the measured dielectric function for solid Ga and previous literature values.

Supporting Information. Experimental dielectric functions for solid and liquid phase gallium, and extracted Ga dielectric functions from the literature sources referenced in this paper, may be obtained as Supplemental Material. This material is available free of charge via the Internet at http://pubs.acs.org.

ACKNOWLEDGEMENTS

The authors thank Prof. Naomi Halas for her support during the early phases of this project and acknowledge the support of the Army's Competitive In-House Laboratory Innovative Research

program. This work is part of the research program of the Foundation for Fundamental Research on Matter (FOM), which is part of the Netherlands Organisation for Scientific Research (NWO), and NanoNextNL, a nanotechnology program funded by the Dutch ministry of economic affairs and the European Research Counsel. The authors acknowledge the SARA Computing and Networking Services (www.sara.nl) for their support in using the Lisa Computer Cluster. A.P. is co-founder/owner of Delmic BV, a company that develops a commercial implementation of the CL system used in this work.

REFERENCES

(1) Moskalyk, R. R. Gallium: The Backbone of the Electronics Industry. *Miner. Eng.* **2003**, *16*, 921–929.

(2) McMahon, J. M.; Schatz, G. C.; Gray, S. K. Plasmonics in the Ultraviolet with the Poor Metals Al, Ga, In, Sn, Ti, Pb, and Bi. *Phys. Chem. Chem. Phys.* **2013**, *15*, 5415–5423.

(3) Naik, G. V; Shalaev, V. M.; Boltasseva, A. Alternative Plasmonic Materials: Beyond Gold and Silver. *Adv. Mater.* **2013**, *25*, 3264–3294.

(4) Hunderi, O.; Ryberg, R. Band Structure and Optical Properties of Gallium. *J. Phys. F Met. Phys.* **1974**, *4*, 2084–2095.

(5) Jezequel, G.; Lemonnier, J. C.; Thomas, J. Optical Properties of Gallium Films between 2 and 15 eV. *J. Phys. F Met. Phys.* **1977**, *7*, 1613–1622.

(6) Wu, P. C.; Kim, T.-H.; Brown, A. S.; Losurdo, M.; Bruno, G.; Everitt, H. O. Real-Time Plasmon Resonance Tuning of Liquid Ga Nanoparticles by in Situ Spectroscopic Ellipsometry. *Appl. Phys. Lett.* **2007**, *90*, 103119.

(7) Wu, P. C.; Khoury, C. G.; Kim, T.-H.; Yang, Y.; Losurdo, M.; Bianco, G. V.; Vo-Dinh, T.; Brown, A. S.; Everitt, H. O. Demonstration of Surface-Enhanced Raman Scattering by Tunable, Plasmonic Gallium Nanoparticles. *J. Am. Chem. Soc.* **2009**, *131*, 12032–12033.

(8) MacDonald, K. F.; Fedotov, V. A.; Pochon, S.; Ross, K. J.; Stevens, G. C.; Zheludev, N. I.; Brocklesby, W. S.; Emel'yanov, V. I. Optical Control of Gallium Nanoparticle Growth. *Appl. Phys. Lett.* **2002**, *80*, 1643–1645.

(9) Ghigna, P.; Spinolo, G.; Parravicini, G. B.; Stella, A.; Migliori, A.; Kofman, R. Metallic versus Covalent Bonding: Ga Nanoparticles as a Case Study. *J. Am. Chem. Soc.* **2007**, *129*, 8026–8033.

(10) Yarema, M.; Wörle, M.; Rossell, M. D.; Erni, R.; Caputo, R.; Protesescu, L.; Kravchyk, K. V.; Dirin, D. N.; Lienau, K.; von Rohr, F.; *et al.* Monodisperse Colloidal Gallium Nanoparticles: Synthesis, Low Temperature Crystallization, Surface Plasmon Resonance and Li-Ion Storage. *J. Am. Chem. Soc.* **2014**, *136*, 12422–12430.

(11) Schön, G. Auger and Direct Electron Spectra in X-Ray Photoelectron Studies of Zinc, Zinc Oxide, Gallium and Gallium Oxide. *J. Electron Spect. Relat. Phenom.* **1973**, *2*, 75–86.

(12) Regan, M. J.; Tostmann, H.; Pershan, P. S.; Magnussen, O. M.; DiMasi, E.; Ocko, B. M.; Deutsch, M. X-Ray Study of the Oxidation of Liquid-Gallium Surfaces. *Phys. Rev. B* **1997**, *55*, 10786–10790.

(13) Langhammer, C.; Schwind, M.; Kasemo, B.; Zoric, I. Localized Surface Plasmon Resonances in Aluminum Nanodisks. *Nano Lett.* **2008**, *8*, 1461–1471.

(14) Szklarska-Smialowska, Z. Pitting Corrosion of Aluminum. *Corros. Sci.* **1999**, *41*, 1743–1767.

(15) Yang, Y.; Callahan, J. M.; Kim, T.-H.; Brown, A. S.; Everitt, H. O. Ultraviolet Nanoplasmonics: A Demonstration of Surface-Enhanced Raman Spectroscopy, Fluorescence, and Photodegradation Using Gallium Nanoparticles. *Nano Lett.* **2013**, *13*, 2837–2841.

(16) Denisyuk, A. I.; Jonsson, F.; MacDonald, K. F.; Zheludev, N. I.; García de Abajo, F. J. Luminescence Readout of Nanoparticle Phase State. *Appl. Phys. Lett.* **2008**, *92*, 093112.

(17) Soares, B. F.; Jonsson, F.; Zheludev, N. I. All-Optical Phase-Change Memory in a Single Gallium Nanoparticle. *Phys. Rev. Lett.* **2007**, *98*, 153905.

(18) Soares, B. F.; MacDonald, K. F.; Zheludev, N. I. Resetting Single Nanoparticle Structural Phase with Nanosecond Pulses. *Appl. Phys. Lett.* **2007**, *91*, 043115.

(19) MacDonald, K. F.; Fedotov, V. A.; Zheludev, N. I. Optical Nonlinearity Resulting from a Light-Induced Structural Transition in Gallium Nanoparticles. *Appl. Phys. Lett.* **2003**, *82*, 1087–1089.

(20) Yi, C.; Kim, T.-H.; Jiao, W.; Yang, Y.; Lazarides, A.; Hingerl, K.; Bruno, G.; Brown, A.; Losurdo, M. Evidence of Plasmonic Coupling in Gallium Nanoparticles / Graphene / SiC. *Small* **2012**, *8*, 2721–2730.

(21) Sanz, J. M.; Ortiz, D.; Alcaraz de la Osa, R.; Saiz, J. M.; González, F.; Brown, A. S.; Losurdo, M.; Everitt, H. O.; Moreno, F. UV Plasmonic Behavior of Various Metal Nanoparticles in the Near- and Far-Field Regimes: Geometry and Substrate Effects. *J. Phys. Chem. C* **2013**, *117*, 19606–19615.

(22) Dogel, S.; Nattland, D.; Freyland, W. Complete Wetting Transitions at the Liquid-Vapor Interface of Gallium-Bismuth Alloys: Single-Wavelength and Spectroscopic Ellipsometry Studies. *Phys. Rev. B* **2005**, *72*, 085403.

(23) Olmon, R. L.; Slovick, B.; Johnson, T. W.; Shelton, D.; Oh, S.-H.; Boreman, G. D.; Raschke, M. B. Optical Dielectric Function of Gold. *Phys. Rev. B* **2012**, *86*, 235147.

(24) García de Abajo, F. J. Optical Excitations in Electron Microscopy. *Rev. Mod. Phys.* **2010**, *82*, 209–275.

(25) Novotny, L.; Hecht, B. *Principles of Nano-Optics*; Cambridge University Press: Cambridge, 2006.

(26) Bharadwaj, P.; Deutsch, B.; Novotny, L. Optical Antennas. *Adv. Opt. Phot.* **2009**, *1*, 438–483.

(27) Wu, P. C.; Losurdo, M.; Kim, T.-H.; Choi, S.; Bruno, G.; Brown, A. S. In Situ Spectroscopic Ellipsometry to Monitor Surface Plasmon Resonant Group-III Metals Deposited by Molecular Beam Epitaxy. *J. Vac. Sci. Technol. B* **2007**, *25*, 1019.

(28) Kuttge, M.; Vesseur, E. J. R.; Koenderink, A. F.; Lezec, H. J.; Atwater, H. A.; García de Abajo, F. J.; Polman, A. Local Density of States, Spectrum, and Far-Field Interference of Surface Plasmon Polaritons Probed by Cathodoluminescence. *Phys. Rev. B* **2009**, *79*, 113405.

(29) García de Abajo, F. J.; Kociak, M. Probing the Photonic Local Density of States with Electron Energy Loss Spectroscopy. *Phys. Rev. Lett.* **2008**, *100*, 106804.

(30) Sapienza, R.; Coenen, T.; Renger, J.; Kuttge, M.; van Hulst, N. F.; Polman, A. Deep-Subwavelength Imaging of the Modal Dispersion of Light. *Nat. Mater.* **2012**, *11*, 781–787.

(31) Knight, M. W.; Liu, L.; Wang, Y.; Brown, L.; Mukherjee, S.; King, N. S.; Everitt, H. O.; Nordlander, P.; Halas, N. J. Aluminum Plasmonic Nanoantennas. *Nano Lett.* **2012**, *12*, 6000–6004.

(32) Coenen, T.; Bernal Arango, F.; Koenderink, A. F.; Polman, A. Directional Emission from a Single Plasmonic Scatterer. *Nat. Commun.* **2014**, *5*, 3250.

(33) Albella, P.; Garcia-Cueto, B.; González, F.; Moreno, F.; Wu, P. C.; Kim, T.-H.; Brown, A.; Yang, Y.; Everitt, H. O.; Videen, G. Shape Matters: Plasmonic Nanoparticle Shape Enhances Interaction with Dielectric Substrate. *Nano Lett.* **2011**, *11*, 3531–3537.

(34) Yamamoto, N.; Ohtani, S.; García De Abajo, F. J. Gap and Mie Plasmons in Individual Silver Nanospheres near a Silver Surface. *Nano Lett.* **2011**, *11*, 91–95.

(35) Nisoli, M.; Stagira, S.; De Silvestri, S.; Stella, A.; Tognini, P.; Cheyssac, P.; Kofman, R. Ultrafast Electronic Dynamics in Solid and Liquid Gallium Nanoparticles. *Phys. Rev. Lett.* **1997**, *78*, 3575–3578.

(36) Lassiter, J. B.; McGuire, F.; Mock, J. J.; Ciracì, C.; Hill, R. T.; Wiley, B. J.; Chilkoti, A.; Smith, D. R. Plasmonic Waveguide Modes of Film-Coupled Metallic Nanocubes. *Nano Lett.* **2013**, *13*, 5866–5872.

(37) García de Abajo, F. J. Transition radiation and surface-plasmon generation by an electron beam. http://nanophotonics.csic.es/widgets/TR/index.html.

(38) Prodan, E.; Radloff, C.; Halas, N. J.; Nordlander, P. A Hybridization Model for the Plasmon Response of Complex Nanostructures. *Science* **2003**, *302*, 419–422.

(39) Knight, M. W.; Wu, Y.; Lassiter, J. B.; Nordlander, P.; Halas, N. J. Substrates Matter: Influence of an Adjacent Dielectric on an Individual Plasmonic Nanoparticle. *Nano Lett.* **2009**, *9*, 2188–2192.

(40) Wu, Y.; Nordlander, P. Finite-Difference Time-Domain Modeling of the Optical Properties of Nanoparticles near Dielectric Substrates. *J. Phys. Chem. C* **2010**, *114*, 7302–7307.

(41) Bernal Arango, F.; Coenen, T.; Koenderink, A. F. Underpinning Hybridization Intuition for Complex Nanoantennas by Magnetoelectric Quadrupolar Polarizability Retrieval. *ACS Photonics* **2014**, *1*, 444–453.

(42) Rebien, M.; Henrion, W.; Hong, M.; Mannaerts, J. P.; Fleischer, M. Optical Properties of Gallium Oxide Thin Films. *Appl. Phys. Lett.* **2002**, *81*, 250–252.

(43) Brandl, D. W.; Oubre, C.; Nordlander, P. Plasmon Hybridization in Nanoshell Dimers. *J. Chem. Phys.* **2005**, *123*, 024701.

(44) Nordlander, P.; Oubre, C.; Prodan, E.; Li, K.; Stockman, M. I. Plasmon Hybridization in Nanoparticle Dimers. *Nano Lett.* **2004**, *4*, 899–903.

(45) Lassiter, J. B.; Aizpurua, J.; Hernandez, L. I.; Brandl, D. W.; Romero, I.; Lal, S.; Hafner, J. H.; Nordlander, P.; Halas, N. J. Close Encounters between Two Nanoshells. *Nano Lett.* **2008**, *8*, 1212–1218.

(46) Mirsaleh-Kohan, N.; Iberi, V.; Simmons, P. D.; Bigelow, N. W.; Vaschillo, A.; Rowland, M. M.; Best, M. D.; Pennycook, S. J.; Masiello, D. J.; Guiton, B. S.; *et al.* Single-Molecule Surface-Enhanced Raman Scattering: Can STEM/EELS Image Electromagnetic Hot Spots? *J. Phys. Chem. Lett.* **2012**, *3*, 2303–2309.

(47) Kneipp, K.; Wang, Y.; Kneipp, H.; Perelman, L. T.; Itzkan, I.; Dasari, R. R.; Feld, M. S. Single Molecule Detection Using Surface-Enhanced Raman Scattering (SERS). *Phys. Rev. Lett.* **1997**, *78*, 1667–1670.

(48) Rycenga, M.; Camargo, P. H. C.; Li, W.; Moran, C. H.; Xia, Y. Understanding the SERS Effects of Single Silver Nanoparticles and Their Dimers, One at a Time. *J. Phys. Chem. Lett.* **2010**, *1*, 696–703.

(49) Li, W.; Camargo, P. H. C.; Lu, X.; Xia, Y. Dimers of Silver Nanospheres: Facile Synthesis and Their Use as Hot Spots for Surface-Enhanced Raman Scattering. *Nano Lett.* **2009**, *9*, 485–490.

(50) Yang, Y.; Akozbek, N.; Kim, T.-H.; Sanz, J. M.; Moreno, F.; Losurdo, M.; Brown, A. S.; Everitt, H. O. Ultraviolet–Visible Plasmonic Properties of Gallium Nanoparticles Investigated by Variable-Angle Spectroscopic and Mueller Matrix Ellipsometry. *ACS Photonics* **2014**, *1*, 582–589.

(51) Wu, P. C.; Losurdo, M.; Kim, T.-H.; Giangregorio, M.; Bruno, G.; Everitt, H. O.; Brown, A. S. Plasmonic Gallium Nanoparticles on Polar Semiconductors: Interplay between Nanoparticle Wetting, Localized Surface Plasmon Dynamics, and Interface Charge. *Langmuir* **2009**, *25*, 924–930.

(52) Choi, S.; Kim, T.-H.; Everitt, H. O.; Brown, A.; Losurdo, M.; Bruno, G.; Moto, A. Kinetics of Gallium Adlayer Adsorption/desorption on Polar and Nonpolar GaN Surfaces. *J. Vac. Sci. Technol. B* **2007**, *25*, 969.

(53) Brenny, B. J. M.; Coenen, T.; Polman, A. Quantifying Coherent and Incoherent Cathodoluminescence in Semiconductors and Metals. *J. Appl. Phys.* **2014**, *115*, 244307.

(54) Lumerical Solutions, Inc. http://www.lumerical.com/.

(55) Palik, E. D. *Handbook of Optical Constants of Solids*; Academic Press: San Diego, CA, 1998; Vol. 3.

(56) Bruggeman, D. A. G. Berechnung Verschiedener Physikalischer Konstanten von Heterogenen Substanzen. I. Dielektrizitätskonstanten Und Leitfähigkeiten Der Mischkörper Aus Isotropen Substanzen. *Ann. Phys.* **1935**, *416*, 636–664.

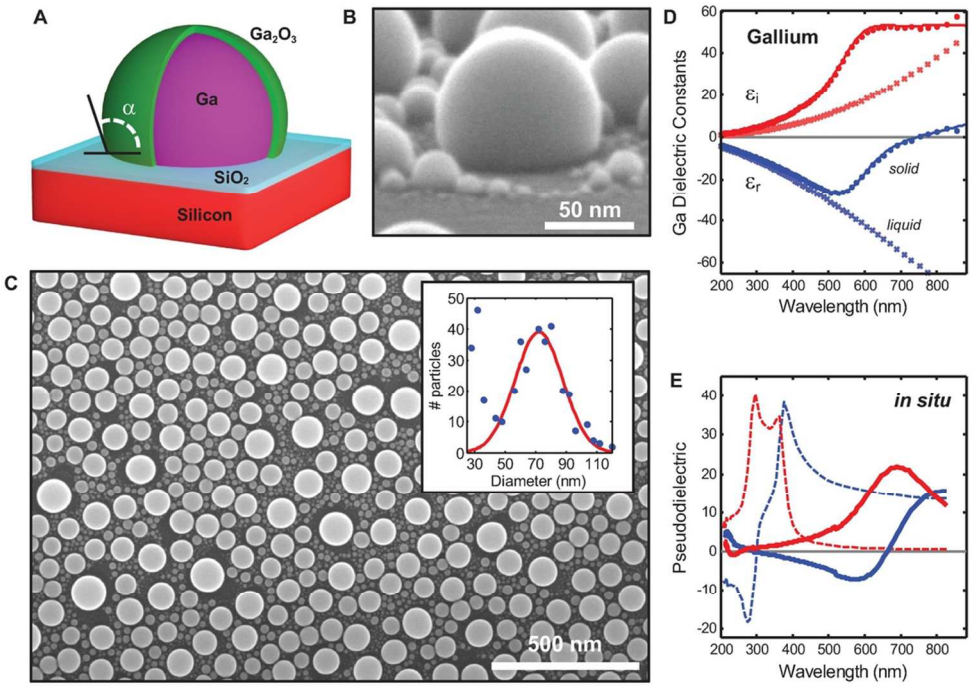

Gallium nanoparticles. **(A)** The geometry of a Gallium nanoparticle can be approximated as a truncated sphere specified by a diameter, contact angle, and oxide thickness. The Si substrate will also have a thin native oxide on the surface. **(B)** Image of a Ga particle taken at 75° tilt with D = 93 nm. **(C)** Typical SEM of a Ga particle array. Inset: the measured size distribution of particles in this image (N = 387) fit with a Gaussian distribution indicating a mean diameter of 72 ± 15 nm. The significant tail for small particles reflects the large number of small Ga particles formed during the fabrication process. **(D)** Experimental dielectric functions of solid Ga (circles) and liquid Ga (crosses), and the multicoefficient FDTD fit used in simulations (lines). **(E)** Pseudodielectric function extracted from ellipsometry measurements on a bare n-Si <111> substrate prior to deposition (dashed lines), and after Ga particle formation (solid lines).
101x71mm (300 x 300 DPI)

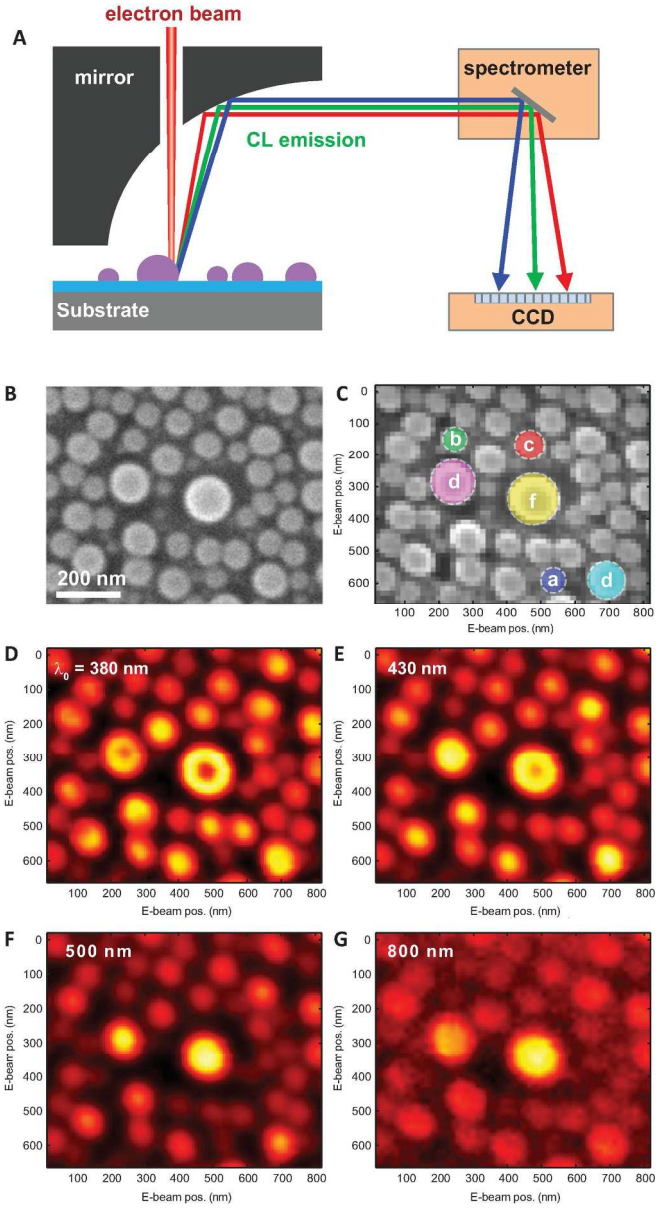

Cathodoluminescence imaging of Ga nanoparticles. **(A)** Schematic of the hyperspectral cathodoluminescence microscopy system. **(B)** Survey scan of the sample area acquired prior to CL imaging. **(C)** Secondary electron image acquired simultaneously with the CL scans. Particles used for subsequent analysis are indicated by letters a-f. From the survey image, the diameters of these particles were determined to be ~40, 60, 80, 100, 120, and 140 ± 5 nm. **(D - G)** CL images at λ = 380, 430, 500, and 800 nm. All images were integrated over a spectral bandwidth of 50 nm, normalized to the full color scale, spatially interpolated for clarity in visualizing the CL distributions.
147x271mm (300 x 300 DPI)

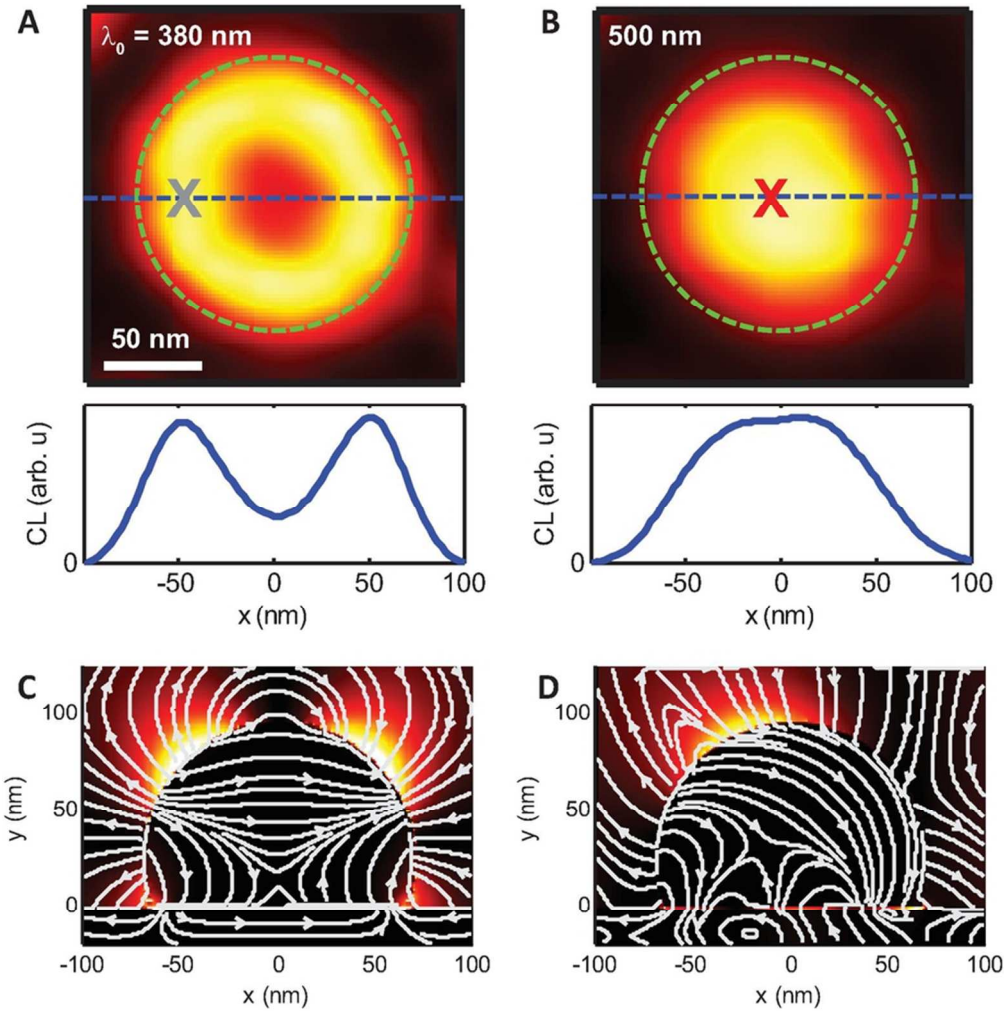

In-plane vs. out-of-plane modes for a D=140 nm Ga NP (particle f). **(A - B)** CL maps showing a characteristic 'annulus' shape for the in-plane modes (λ=380 nm), and a single maximum for the out-of-plane dipolar modes (λ=500 nm). Crosscuts show normalized field intensities across the particle center (cut position: dashed blue lines). Positions marked by X indicate locations at which nearly pure in-plane or out-of-plane modes may be excited and representative emission spectra can be extracted. **(C - D)** Calculated field maps of Ez^2, which correspond to the experimental maps, are shown at the calculated peak intensities of these modes for (C) normal incidence excitation with λ = 270 nm and (D) a p-polarized wave with λ = 470 nm and at 70° off-normal incidence. Electric field lines are shown in white.
77x78mm (300 x 300 DPI)

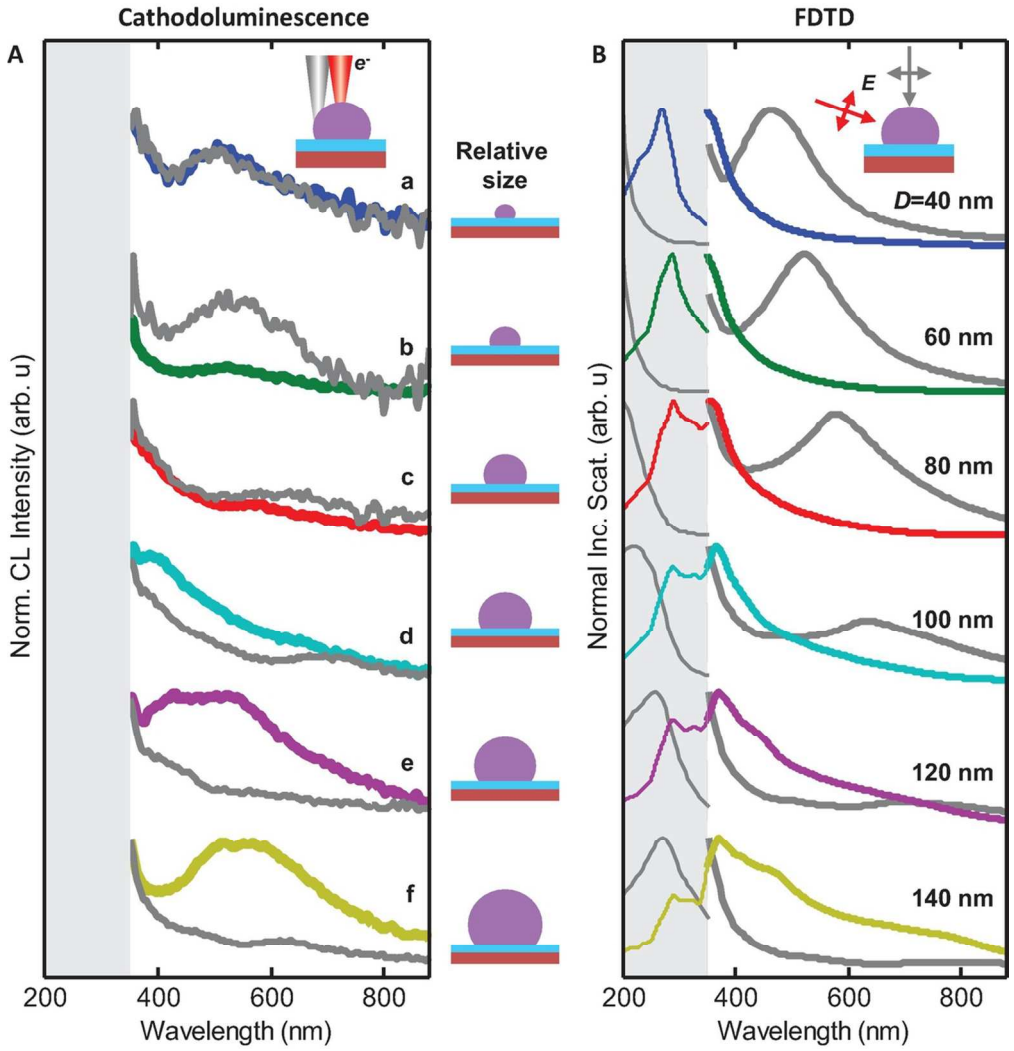

CL spectra of Ga particles. **(A)** Experimental CL spectra for excitation either at the side of the particle (grey lines) or the center of the particle (colored lines). The shadowed area indicates the spectral region inaccessible to the CL detector. **(B)** Spectra calculated for the experimental particle dimensions using FDTD with plane-wave excitation at either normal incidence (grey lines) or grazing incidence (70°, colored lines). All spectra are offset for clarity: thick lines are normalized within the experimental data range, and thin lines are normalized within the λ = 200 – 350 nm UV spectral range (shaded region).
107x112mm (300 x 300 DPI)

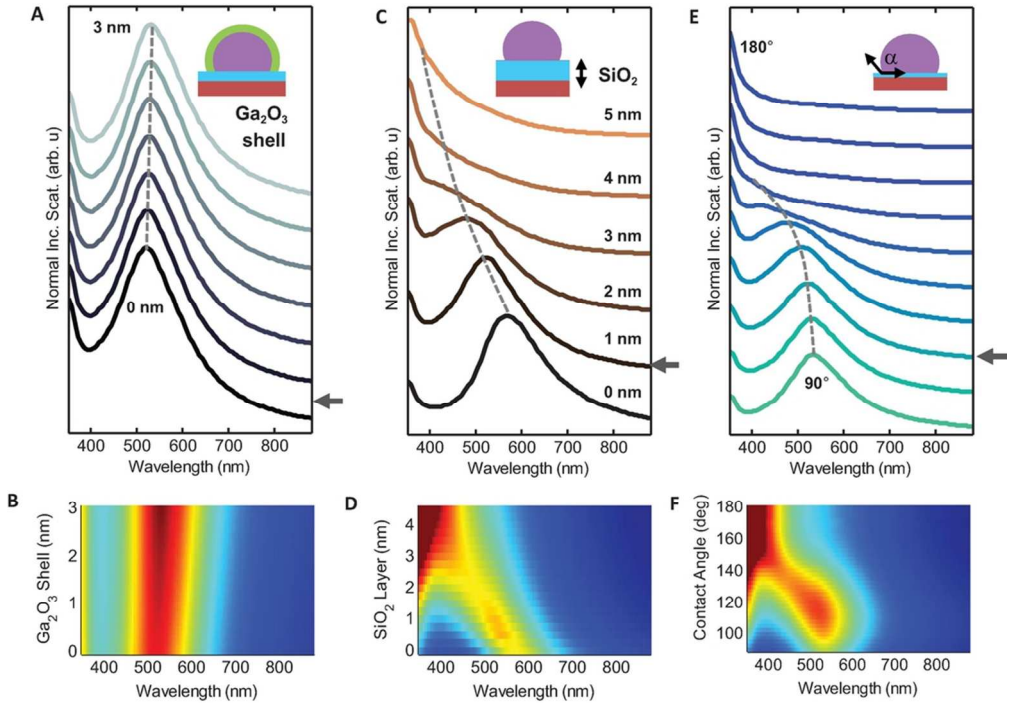

Spectral influence of Ga particle parameters: oxide shell thickness, substrate oxide thickness, and contact angle. Spectra were calculated for a D = 60 nm Ga particle using normal incidence excitation. **(A - B)** Effect of the oxide shell thickness, calculated for 0 nm (unoxidized) to 3 nm with a 1 nm layer of SiO_2 on the Si substrate and a 110° contact angle. **(C - D)** Effect of the native oxide layer on the Si substrate, calculated for 0 – 5 nm, no Ga_2O_3 shell, and a 110° contact angle. **(E - F)** Influence of contact angle on the Ga spectrum, calculated for angles between 90° (a hemisphere) and 180° (a perfect sphere). The substrate oxide was set at 1 nm, with no Ga_2O_3 shell. Dashed grey lines are provided as a guide to the eye. Grey arrows indicate the parameters used to calculate the NP resonances shown in Figures 3 and 4.
90x63mm (300 x 300 DPI)

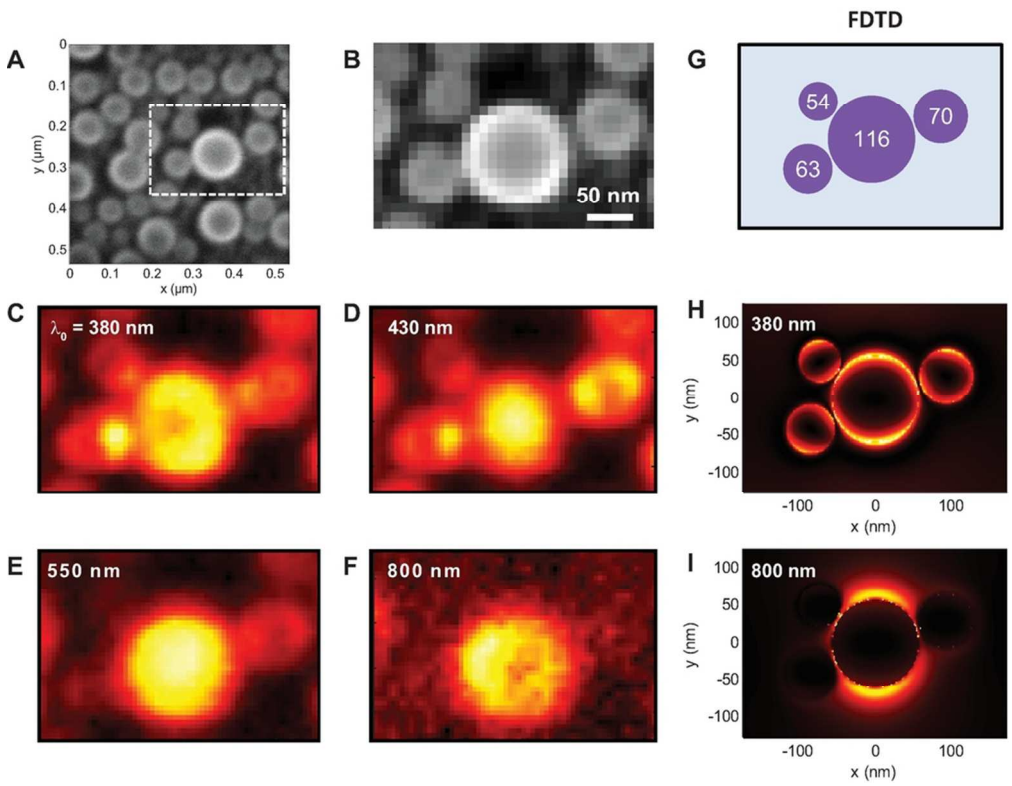

Hybridization in Ga plasmons. **(A)** Survey image with the scan area indicated by the white dashed box. **(B)** Simultaneously acquired SE image of the Ga NP cluster. **(C - F)** CL maps of the cluster at λ = 380, 430, 550, and 800 nm, with an integration bandwidth of 50 nm. **(G)** Simulation geometry, with particle dimensions indicated. **(H - I)** Simulated in-plane field maps showing polarization-averaged E_z^2. Asymmetries in the field profiles correspond with the CL maps and indicate interparticle interaction.
86x66mm (300 x 300 DPI)